Prepared for submission to JCAP

Constraints on WIMP and Sommerfeld-Enhanced Dark Matter Annihilation from HESS Observations of the Galactic Center

Kevork N. Abazajian[a] **J. Patrick Harding**[a,b]

[a]Center for Cosmology, Department of Physics & Astronomy, University of California, Irvine, CA 92697

[b]Maryland Center for Fundamental Physics, Department of Physics, University of Maryland, College Park, MD 20742-4111

E-mail: kevork@uci.edu, hard0923@umd.edu

Abstract. We examine the constraints on models of weakly interacting massive particle (WIMP) dark matter from the recent observations of the Galactic Center by the High Energy Spectroscopic System (HESS) telescope. We analyze canonical WIMP annihilation into Standard Model particle final states, including $b\bar{b}$, $t\bar{t}$ and W^+W^-. The constraints on annihilation into $b\bar{b}$ is within an order of magnitude of the thermal cross section at $\sim$3 TeV, while the $\tau^+\tau^-$ channel is within a factor of $\sim$2 of thermal. We also study constraints on Sommerfeld-enhanced dark matter annihilation models, and find that the gamma-ray observational constraints here rule out all of the parameter space consistent with dark matter annihilation interpretations of PAMELA and the Fermi-LAT e^+e^- spectrum, in specific classes of models, and strongly constrains these interpretations in other classes. The gamma-ray constraints we find are more constraining on these models, in many cases, than current relic density, cosmic microwave background, halo shape and naturalness constraints.

Keywords: dark matter theory, dark matter experiments, gamma ray experiments

ArXiv ePrint: arXiv:1110.6151

Contents

1 Introduction

The existence of cosmological dark matter has been well-established by observations of galaxy clusters, galaxy rotation curves, the cosmic microwave background (CMB), and large-scale cosmological structure. However the identity of the dark matter has remained a fundamental unsolved problem in cosmology and particle physics for nearly 80 years [1]. Several particle candidates have been proposed that could account for the dark matter (for a review, see, e.g. [2]). One well-motivated dark matter candidate is a weakly-interacting massive particle (WIMP), which can naturally produce a relic abundance at the observed dark matter density. Thermal production of dark matter prefers a scale of the dark matter cross-section at $\langle \sigma_{\rm A} v \rangle \approx 3 \times 10^{-26}$ cm^3 s^{-1}. This annihilation rate into Standard Model particles results in energetic gamma-ray production through the hadronization of quarks, bremsstrahlung of leptons, or directly into two gammas through higher-order processes. This leads to the so-called method of "indirect detection" of dark matter, constraining the dark matter mass, annihilation cross-section, and annihilation spectrum through a search for the Standard Model byproducts of WIMP annihilation.

The High Energy Stereoscopic System (HESS) telescope has strong sensitivity to high-energy gamma-rays such as those from high-mass WIMPs [3]. HESS consists of an array of atmospheric Čerenkov telescopes in Namibia designed to search for high-energy gamma-rays, with 960 pixels per telescope at a resolution of 0.16° per pixel [4]. Specifically, HESS is sensitive to gamma-ray energies from a few hundred GeV to a few tens of TeV. Previously, studies of the Galactic Ridge for $|\ell| < 0.8°$ and $|b| < 0.3°$ by HESS [5] have been used to limit the dark matter cross-section at high masses (0.5-30 TeV) [6–13]. However, an even more stringent constraint on the dark matter cross-section has been shown to come from a new analysis of a region around the Galactic Center (GC) [3]. Here, we analyze in detail the constraints arising from this observation.

The HESS GC analysis uses a reflected background technique to provide a robust background region for the gamma-ray signal from the GC. Because the background region is further from the GC than the source region, it is expected that the dark matter signal should be larger in the source region than the background region, for a dark matter halo profile whose density peaks toward the GC. The HESS GC analysis shows no excess gamma-ray

signal in the source region over the background region. Therefore, any dark matter annihilation signal must produce few enough gamma-rays that the gamma-ray flux in the source region is indistinguishable from the gamma-ray flux in the background, at the current HESS sensitivity.

There have recently been stacked studies of the gamma-ray signals coming from dwarf spheroidal galaxies by the Fermi-LAT which have been used to constrain WIMP annihilation cross-sections and, in particular, have excluded thermal low-mass WIMPs in the $b\bar{b}$ and $\tau^+\tau^-$ annihilation channels below ~ 30 GeV [14, 15]. Here, we show that the HESS GC analysis provides much tighter constraints than the stacked Fermi-LAT dwarf spheroidals for dark matter masses above the Fermi-LAT energy window.

There remains interest in the possibility of dark matter annihilation as the source of the excess cosmic ray positron fraction at $\sim$ 10-100 GeV observed by the PAMELA satellite, with e^+e^- pairs produced either directly or indirectly in a dark matter particle pair annihilation cascade [16–19]. Additionally, features in the higher-energy 10^2 to 10^3 GeV e^+e^- spectrum seen by the Fermi-LAT [20] are also consistent with the dark matter annihilation interpretations of the lower energy positron excess data [10, 21, 22]. A recent study of the e^+e^- data from the Fermi-LAT is consistent with the positron excess of the PAMELA satellite and shows the spectrum continuing to rise up to at least ~ 200 GeV [23].

In order to achieve the dark matter annihilation rate required for these e^+e^- signals while remaining consistent with the expected thermal production cross section, and to avoid an excess in anti-proton observations (which is not seen), the annihilation rate can be enhanced through a low-energy Sommerfeld-enhancement and limited to leptonic modes with a light (< 1 GeV) dark-force carrying particle [24–27]. Such an enhanced cross-section from a new force is in tension with detailed calculations of the relic abundance of the dark matter, so that such a candidate in many cases may not contribute to all of the dark matter [28–32]. Such candidates are also constrained by non-thermal distortions of the CMB [29, 33–35] and asphericity observed in dark matter halos [30, 31]. Cases of these models remain viable given all such constraints [36, 37]. There are also constraints on these models from the observed diffuse gamma-ray and X-ray backgrounds [38, 39], observations toward the GC by Fermi-LAT [68], as well as big-bang nucleosynthesis [40, 41].

One model of dark matter with a light dark-force carrying particle and Sommerfeld-enhanced cross-section is "eXciting dark matter" (XDM) [24, 42]. XDM was initially proposed to explain the 511 keV gamma-ray signal from the GC (see ref. [43] for a discussion of these signals). In XDM, there are two lowest-energy dark states χ and χ^* which have masses differing by only a few MeV, with a light gauge bosons ϕ mediating excitations from χ to χ^*. The exchange of many gauge bosons leads to a Sommerfeld-enhanced cross-section much larger than that of a thermal relic. The annihilation $\chi\chi \to \phi\phi$ followed by the decay of ϕ into leptons leads to an excess of high-energy electrons and positrons in the GC. This scenario has also been considered to explain the excess in local positrons seen by the PAMELA and Fermi-LAT satellites. Most recently, ref. [36] has interpreted the XDM explanation for the PAMELA and Fermi-LAT excesses including constraints from the thermal relic density, CMB, self-interaction bounds, and naturalness bounds. Below, we compare the gamma-ray constraints from the HESS GC analysis to these other XDM limits.

The sensitivity of the HESS GC observation to dark matter annihilation, as with all Galactic Center observations, depends on the nature of the dark matter density profile. Specifically, for the HESS GC background subtraction method, there must be a higher dark matter density within the inner $\lesssim$150 pc, in the signal region, than the background subtrac-

tion region between approximately 150 pc and 450 pc. As pointed out also in the HESS Collaboration analysis [3], if there exists a constant-density core within the inner ∼450 pc of the Milky Way, no limits on dark matter annihilation can be derived from the HESS GC observation since the background subtraction would also remove any equivalent signal.

There is significant debate in the literature as to the nature of the inner dark matter profile of a galaxy such as the Milky Way. Numerical simulations are employed in attempts to accurately determine the inner dark matter density profile. The canonically-adopted dark matter halo density profile for the case of cold dark matter is the r^{-1} inner-radius scaling Navarro-Frenk-White (NFW) profile [44]. The highest spatial resolution simulations of Milky-Way-type halo formation are pure dark matter halo simulations: Via Lactea II [45], GHALO [46] and AQUARIUS (A-1) [47] (which have gravitational softening lengths of 40, 61 and 20 pc, respectively), which find a peaked density profile down to ∼100 pc, with a logarithmically-changing slope that is sometimes dubbed an "Einasto" profile. The vast majority of studies that include baryons in addition to dark matter have found that baryonic effects concentrate and steepen the central dark matter distribution due to adiabatic contraction [48, 49], including recent high-resolution simulations with gas cooling, star formation, and stellar feedback processes [50–53]. Importantly, ref. [53] does an extensive error analysis of their numerical results. In contrast, some studies' simulations have claimed that baryonic effects may have the opposite effect, reducing the dark matter density in the central region via dark matter expansion from stellar and gas feedback outflows, and producing flat or nearly-flat density cores at up to 2-3 kpc in size for an approximately Milky Way size halo, fit by cored isothermal or Burkert profiles [54–56]. It has been shown in ref. [57] that the S2 or Plummer force softening must be a factor of ≈5 times smaller than the scale of interest for the inner profile of dark matter halos in order to achieve greater than 5% accuracy in radial accelerations of particles, with an ideal time-step algorithm choice. Poor force resolution has been shown to generally lead to artificially lower central densities [58]. The gravitational softening length used in the simulations in ref. [55] is 0.5 kpc, so it is questionable to draw conclusions at the claimed ∼kpc core scale. In the recent work of ref. [56], the gravitational softening length is 0.3125 kpc [59], and therefore conclusions of the inner 1-2 kpc are also difficult to make with confidence. Furthermore, ref. [56] finds evidence for a core to be produced only in the more extreme feedback High Feedback Run, while the Low Feedback Run found adiabatic contraction that steepened the dark matter profile.

In summary, work indicating the presence of dark matter density cores in numerical simulations are at the edge of their resolution limits. It is important to consider that if it becomes firmly established from numerical simulations that there is necessarily a constant-density core in the Milky Way at the $\gtrsim$ 450 pc scale, then the HESS GC limits presented here are not applicable due to the observation's background subtraction method. This was also noted by the HESS collaboration work [3]. However, at this time robust numerical simulations predominantly indicate contraction and steepening of the central density profile due to baryonic effects, and the adoption of the non-contracted NFW or Einasto profile here is conservative relative to the steeper profiles.

Below we show that, in the case of a non-adiabatically-contracted NFW or Einasto dark matter halo profile, the HESS GC observation provides a strong limit on the cross-section of high-mass WIMPs' annihilation into several Standard Model channels. Furthermore, we show how the dark matter annihilation interpretation of the PAMELA excess and Fermi-LAT e^+e^- feature signals is excluded at above 95% CL in many cases. Dark matter interpretations of these signals are in tension with the HESS GC observations for two-body standard model

particle final states and gauge-boson mediated four-lepton final states, when also including the constraints for Fermi-LAT observations toward local dwarf galaxies. Importantly, the HESS limits presented here for XDM are more constraining than the thermal relic density, CMB, self-interaction bounds, and naturalness bounds.

2 Data Analysis

The data used in this paper comes from the HESS collaboration analysis of the GC from ref. [3]. The events analyzed are those from 112 hours of live time from the HESS very-high energy gamma-ray instrument with zenith angles smaller than 30° which were within the central 4° of the HESS field-of-view. Contamination of the dark matter signal due to the Galactic plane is excluded by masking the regions with Galactic latitude $|b| < 0.3°$ and an additional mask within 0.3° of the extended source HESS J1745–303 ($(b, \ell) = (-0.6°, 358.71°)$) [60].

The source region is defined by $0.02° \times 0.02°$ pixels that lie within 1° of the GC, do not lie within the mask, and have a well-defined background. The background region is determined by choosing a telescope pointing position within 1.5° of the GC and rotating each pixel in the source region (with masked pixels removed) by 90°, 180°, and 270° about the telescope pointing position. Any of these pixels which is further than 1° from the GC and does not lie within the mask is considered background. Pixels within the inner 1° for which there are no corresponding background pixels are excluded from the analysis. This process was then repeated for multiple telescope pointing positions, calculating the differential flux in both the background and source regions. For additional details on the HESS GC analysis, see ref. [3].

3 Dark Matter Annihilation Limits from the HESS GC Observations

3.1 Gamma-Ray Emission from Annihilating Dark Matter

A robust calculation of the expected final state radiation from dark matter annihilation requires accurate quantification of the dark matter source as well as the products in the final state gamma-ray radiation chain. The differential flux per solid angle for a dark matter candidate with cross-section $\langle \sigma_{\rm A} v \rangle$ over a solid angle $\Delta\Omega$ is

$$\frac{dF}{dE} = \frac{\langle \sigma_{\rm A} v \rangle}{2} \frac{J_{\Delta\Omega}}{J_0} \frac{1}{4\pi M_\chi^2} \frac{dN_\gamma}{dE} \ , \tag{3.1}$$

where dN_γ/dE is the gamma-ray spectrum per annihilation and M_χ is the dark matter particle mass. The integrated mass density squared along line-of-sight x, averaged over the solid angle of the observation region $\Delta\Omega$ is defined as

$$J_{\Delta\Omega} = \frac{J_0}{\Delta\Omega} \int_{\Delta\Omega} d\,\Omega \int d\,x\ \rho^2(r_{\rm gal}(b, \ell, x)) \ , \tag{3.2}$$

where distance from the GC is given by

$$r_{\rm gal}(b, \ell, x) = \sqrt{R_\odot^2 - 2xR_\odot \cos(\ell)\cos(b) + x^2} \ . \tag{3.3}$$

A normalization constant $J_0 \equiv 1/\left[8.5 \text{ kpc}(0.3 \text{ GeV cm}^{-3})^2\right]$ is chosen to make J dimensionless, but the final flux calculation is independent of the choice of J_0. The coordinates b and ℓ are the Galactic latitude and longitude, respectively. Following the HESS Collaboration, the

dark matter profiles $\rho(r)$ we choose are the non-adiabatically-contracted Einasto and NFW models of ref. [61] with the local dark matter density $\rho_\odot \equiv 0.389$ GeV cm^{-3} (0.385 GeV cm^{-3}) for an NFW (Einasto) profile [62]. Since there were several telescope pointing positions not given explicitly in ref. [3], we cannot and did not independently calculate $\bar{J}_{\Delta\Omega}$ but adopt those of the HESS Collaboration. Importantly, as discussed in the introduction and in the HESS Collaboration study, in the case of a cored-isothermal or Burkert profile with a constant-density core that extends at or beyond ∼450 pc, then the background subtraction region would have an identical annihilation signal as the signal region, and no constraint can be placed on dark matter annihilation by this method. We have checked that the J-values for the single pointing shown in figure 2 of ref. [3] are approximately their $\bar{J}$'s. Averaging over telescope pointing positions, the HESS analysis calculated the dark matter J-values for the source ($\bar{J}_{\rm s}$) and background ($\bar{J}_{\rm b}$) regions using the NFW and Einasto profiles [3]:

$$\bar{J}_{\rm s}^{\rm NFW} = 1604 \tag{3.4}$$

$$\bar{J}_{\rm b}^{\rm NFW} = 697 \tag{3.5}$$

$$\bar{J}_{\rm s}^{\rm Einasto} = 3142 \tag{3.6}$$

$$\bar{J}_{\rm b}^{\rm Einasto} = 1535 \ . \tag{3.7}$$

Note that toward the GC we adopt zero astrophysical substructure boost. However, there may be a substructure contribution to the flux of order 4% to 0.04% in the inner ∼1° view of the GC [63].

3.2 Calculation of Dark Matter Spectra

To calculate the photon spectrum for a particular WIMP annihilation channel, we use PYTHIA 6.4 to simulate the photon radiation of charged particles as well as decays of particles such as the π^0 [64]. Specifically, we run PYTHIA to simulate an e^+e^- collision at a center of mass energy of $2M_\chi$ through a Z' to a final state that corresponds to the annihilation products of the dark matter. For WIMP annihilation to final states through light gauge bosons (such as the $4e$ and 4μ channels) we have the Z' decay into two scalar (H_0) states, each of which annihilates into two leptons. For the XDM case, we employ a light gauge boson which has branching fraction to e^+e^-, $\mu^+\mu^-$, and $\pi^+\pi^-$ set by the particular XDM model. For the models with light gauge bosons, photons can only be radiated at fairly low energy in the gauge boson rest frame. Therefore, in the center-of-mass frame of the dark matter annihilation, the average number of hard photons is significantly reduced in comparison to direct annihilation to a two-body standard model final state.

We turn off initial state radiation such that all photons only come from the radiation or decay of the dark matter annihilation products. We turn on the decays of particles which are not decayed with the default PYTHIA settings, namely muons, charged pions, and charged kaons. Additionally, we turn on the muon decay channel $\mu^- \to e^-\nu_\mu\bar{\nu}_e\gamma$, with the standard branching fraction of 0.014 [65]. Using a large sample of events for each final state and each value of M_χ, the number of photons in the final state in a given logarithmic energy bin is counted and averaged over the number of events, yielding the average number of photons in that energy bin per annihilation event.

For WIMP annihilation to final states through extremely light gauge bosons ($m_\phi \lesssim 0.5$ GeV), the PYTHIA calculation becomes impractical due to low-energy cutoffs for radiation processes. For such annihilation channels (with $m_\phi = 0.25$ GeV and $m_\phi = 0.35$ GeV) we instead use the analytic formulae given in Appendix A of ref. [66]. For the $4e$ state, all

photons come from radiation off the final electrons and positrons. For the 4μ state, photons come from radiation off the final electrons and positrons as well as the radiation from the muons before they decay. We have verified the analytic spectra model by comparison to PYTHIA spectra for heavier gauge bosons.

3.3 Limits on the Dark Matter Annihilation Cross-Section

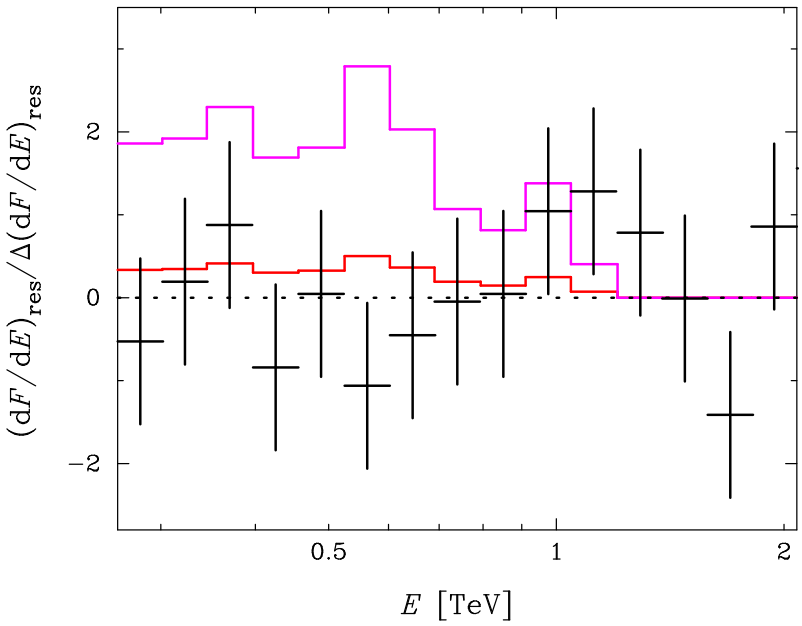

Figure 1. Shown are the data from the HESS GC observation, for which the signal and background are consistent with no difference in flux at the level of $\chi^2/\mathrm{DOF} = 0.75$. For comparison, two possible dark matter signals are shown as well. Both dark matter signals are for a 1.2 TeV WIMP annihilating via 0.25 GeV gauge bosons into two e^+e^- pairs, for an NFW halo profile. The red (lower) histogram is the signal expected for a dark matter cross-section $\langle\sigma_{\mathrm{A}}v\rangle = 9 \times 10^{-25}$ cm^3 s^{-1}, which has a total $\Delta\chi^2 = 2.79$. The magenta (upper) histogram is the signal expected for a dark matter cross-section $\langle\sigma_{\mathrm{A}}v\rangle = 5 \times 10^{-24}$ cm^3 s^{-1} and mass $M_\chi = 1.2$ TeV, with a $\Delta\chi^2 = 41.2$. These signals correspond with the upper end of the red Fermi-LAT plus PAMELA region, and lower end of the purple rectangle in figure 4(a), in the case of assuming a subdominant substructure contribution, and are excluded at greater than 95% CL. Note that the HESS GC observation extends to higher energies than shown here.

Figure 3 of ref. [3] shows the observed source and background fluxes in 35 energy bins from 0.28 to 31 TeV. The two regions are consistent with each other, with zero difference in flux having a $\chi^2/\mathrm{DOF} = 0.75$. Therefore, any dark matter signal must be small enough that the source region does not have appreciably greater gamma-ray flux, within errors, than the background region. Figure 1 illustrates the difference between the lack of a dark matter signal from HESS and two representative dark matter signals. Using the dark matter J-values from eqs. 3.4–3.7, we have derived 95% one-sided confidence-level (CL) (corresponding with a 90% two-sided CL) constraints on the dark matter cross-section as a function of mass for several key annihilation channels, using the total χ^2 in all bins.

In the figures, the light blue cross-hatched region is excluded at 95% CL for both the NFW and Einasto dark matter profiles. The singly-hatched light blue regions are excluded

at 95% CL for the Einasto profile but not for the more conservative NFW profile. The purple regions are the 95% CL limits from a combined analysis of ten dwarf spheroidal galaxies from the Fermi-LAT Collaboration [15]. In particular, note that in figure 2(a) and figure 3(b) we have extended the mass of the dark matter down to 10 GeV in order to show the exclusion of a standard thermal relic below 27 GeV (37 GeV) for the $b\bar{b}$ ($\tau^+\tau^-$) annihilation channel by the Fermi-LAT stacked analysis of dwarf galaxies [15]. The dark pink regions represent the annihilation cross-section for a thermal relic, $\langle\sigma_{\rm A}v\rangle \approx 3\times10^{-26}$ cm^3 s^{-1}. The dark matter constraints for the standard WIMP annihilation channels $b\bar{b}$, $t\bar{t}$, and W^+W^- are shown in figure 2. We show the $t\bar{t}$ channel since this should dominate for high mass dark matter ($M_\chi \gtrsim 200$ GeV). Our $b\bar{b}$ constraints are consistent with the quark channel limits from HESS [3]. As a comparison to the thermal cross-section, figure 2(c) also includes the expected cross-section for a non-thermal wino-like neutralino (the dashed red line) [67].

Figure 3 shows the dark matter limits for dark matter annihilating directly into leptons, whereas in figure 4, the dark matter annihilates into two gauge bosons ϕ of mass $m_\phi = 0.25$ GeV which then decay into leptons. (Note that the $4e$ case requires an *ad hoc* requirement of gauge boson decay into electrons and not muons. Neither the constraints nor signals would be significantly different in the case of, e.g., $m_\phi = 0.2$ GeV, where annihilation to e^+e^- would be energetically required.) Heavy dark matter masses annihilating primarily into leptons are particularly interesting in the context of the PAMELA positron excess [16] and the e^+e^- feature seen by the Fermi-LAT [20]. Such leptonic annihilation channels with a cross-section much larger than that of a thermal relic have been studied as the source of these anomalies [10, 22]. In figures 3 and 4 we have included one dark matter annihilation interpretation of the PAMELA excess in light pink and the analogous interpretation of the Fermi-LAT feature in red [10]. Recent analysis of the positron fraction by the Fermi-LAT Collaboration consistent with the PAMELA excess continues to rise up to energies of 180 GeV bin center energy, ruling out PAMELA regions below $M_\chi \approx 160$ GeV from being consistent with dark matter annihilation [23]. In figures 3(a) and 4(b) we include fits to the interpretation of the PAMELA excess in light green outline and the Fermi-LAT e^+e^- feature in dark green outline from ref. [22]. In panel 4(b), for the NFW profile case, we exemplify the strength of the limit by plotting the 95%, 99.7%, and 99.9999% CL limits as dashed, dot-dashed and solid lines, respectively.

In figure 5 three benchmark XDM models which are consistent with a combination of the PAMELA signal and the Fermi-LAT feature are shown, with red representing the 68% CL region and light pink representing the 95% CL region. Figure 5(a) contains the regions for annihilations which go 50% into e^+e^- and 50% into $\mu^+\mu^-$ through two intermediate gauge bosons of mass $m_\phi = 0.35$ GeV; figure 5(b) contains the regions for annihilations which go 33% into e^+e^-, 33% into $\mu^+\mu^-$, and 33% into $\pi^+\pi^-$ through two intermediate gauge bosons of mass $m_\phi = 0.58$ GeV; and figure 5(c) contains the regions for annihilations which go 25% into e^+e^-, 25% into $\mu^+\mu^-$, and 50% into $\pi^+\pi^-$ through two intermediate gauge bosons of mass $m_\phi = 0.90$ GeV.

When comparing to signal-fit regions from other work, a scaling of $\rho_0^2/\rho_\odot^2$ has been done to normalize that work's local dark matter density ρ_0 to the one adopted here. In the literature, signals for the PAMELA and Fermi-LAT excesses are ascribed boost factors for dark matter annihilation that can include both astrophysical substructure boosts and particle physics boosts, as well as the enhancement of latter due to the former. The local boost can be separated as $B_{\rm local} = B_s B_p$ into the substructure boost B_s and the particle boost B_p (when ignoring the enhancement of the latter to to the former). To be clear and

conservative, we employ a relatively strong local substructure boost, $B_s = 1.57$, using that expected from unresolved substructure calibrated to the Via Lactea II simulations [38, 69]. We incorporate the fit regions from ref. [22] such that

$$E_F = \left(\frac{\rho_\odot}{0.3 \text{ GeV cm}^{-3}}\right)^2 B_s B_p \ . \tag{3.8}$$

Both $B_{\rm local}$ and E_F designate the scaling factor from $\langle \sigma_{\rm A} v \rangle = 3 \times 10^{-26}$ cm^3 s^{-1}, as shown in our figures.

Relative boosts between the GC and local effects can alter the relative constraints between the annihilation in the GC versus local cosmic ray signals in Sommerfeld-enhanced annihilation models, where Sommerfeld-enhancement is greater in low-velocity substructures. As discussed in ref. [37], the boost toward the GC relative to the local is

$$\frac{B_{\rm GC}}{B_{\rm local}} = \frac{S_{v(r=0)}/S_{v\sim 150 \text{ km/s}}}{1 + (S_{v\to 0}/S_{v\sim 150 \text{ km/s}})\Delta(8.5 \text{ kpc})}, \tag{3.9}$$

where S is the Sommerfeld-enhancement in a given model at a distance r from the GC, for a given velocity dispersion of the dark matter v. Here, $\Delta \equiv 1 - B_s$, which we take to be $\Delta(8.5 \text{ kpc} = 0.57$.

For specificity, we adopt $m_\phi = 0.25$ GeV, which corresponds to $S_{v\to 0}/S_{v\sim 150 \text{ km/s}} \approx 5$, from figure 1 of ref. [37]. This model is a $4e$ channel case shown in figure 4(a). The purple rectangle shows the range of annihilation cross sections for a 1.2 TeV Sommerfeld-enhanced scenario consistent with the thermal relic density, the CMB, self-interaction bounds, and naturalness, for Δ from 10^{-4} to unity, corresponding to $B_{\rm local}$ from 30 to 300 [37]. The scaling of the signal toward the GC relative to the local boost is set explicitly by the local substructure boost Δ, and the value of $S_{v(r=0)}$, which is determined by the velocity dispersion of dark matter in the ∼450 pc of the HESS observation of the GC (and *not* exactly at $r = 0$). It has been shown that the dark matter velocity rapidly decreases toward the GC in Milky Way scale halos [70], and the limit $v \to 0$ is potentially appropriate for $S_{v(r=0)}$, which we adopt in one case of our limits. In this GC low velocity limit case, one can take the substructure dominant versus subdominant cases:

$$\frac{B_{\rm GC}(v \to 0)}{B_{\rm local}} \approx \begin{cases} 5 & (\Delta = 10^{-4}), \\ 0.83 & (\Delta = 1). \end{cases} \tag{3.10}$$

Baryonic effects have been found to enhance the velocity of the dark matter toward the GC to make it comparable or greater than to that at the solar distance [50, 71], such that $S_{v(r=0)} \approx S_{v\sim 150 \text{ km/s}}$ [72], and in that scenario the substructure limiting cases are:

$$\frac{B_{\rm GC}(v \sim 150 \text{ km s}^{-1})}{B_{\rm local}} \approx \begin{cases} 1 & (\Delta = 10^{-4}), \\ 0.17 & (\Delta = 1). \end{cases} \tag{3.11}$$

We designate these ranges of constraints as bars and arrows for the corresponding four cases in figure 4(a), with the $v \to 0$ GC in green and $v \sim 150$ km s^{-1} GC in dark blue.

Ref. [37] claims that $\Delta(8.5 \text{ kpc})/\Delta(r = 0) \sim 20$ is relevant for the comparative constraints between the GC and the local boost, which strictly is only the case for strong local substructure domination and high velocities in the GC. More generally, it is eq. (3.9) and the local substructure boost that sets the scaling, and is what we adopt. Note that any substructure in the dark matter of the GC region would enhance the constraints here. We ignore this enhancement to be conservative, i.e., we only include the annihilation from the smooth component in the GC region.

3.4 Discussion

For the $b\bar{b}$ annihilation channel (figure 2(a)), the HESS GC constraints are stronger than the constraints from the Fermi-LAT analysis of dwarf spheroidal galaxies for $M_\chi \gtrsim 900$ GeV when adopting a non-cored Einasto or NFW dark matter profile. The limits on this channel for an Einasto dark matter profile are within an order of magnitude of the thermal cross-section for 2 TeV $\lesssim M_\chi \lesssim 5$ TeV. Similarly, the W^+W^- annihilation channel (figure 2(c)) has stronger constraints than the Fermi-LAT dwarfs for $M_\chi \gtrsim 800$ GeV and limits $\langle \sigma_A v \rangle \leq 3 \times 10^{-25}$ cm^3 s^{-1} for 1 TeV $< M_\chi <$ 6 TeV. The $t\bar{t}$ annihilation channel (figure 2(b)) has somewhat weaker constraints, limiting $\langle \sigma_A v \rangle \leq 5 \times 10^{-25}$ cm^3 s^{-1} for 2 TeV $< M_\chi <$ 10 TeV.

The light pink PAMELA excess region of ref. [10] and the light green PAMELA excess region of ref. [22] are both excluded above $M_\chi \sim 400$ GeV by the HESS GC data for the $\mu^+\mu^-$ annihilation channel (figure 3(a)) when adopting a non-cored Einasto or NFW halo model. Also for the $\mu^+\mu^-$ channel, the red Fermi-LAT feature region of ref. [10] and the dark green Fermi-LAT feature region of ref. [22] are excluded by the HESS GC data when adopting either halo model.

In the $\tau^+\tau^-$ annihilation channel (figure 2(b)), the HESS GC observation excludes a cross-section of $\langle \sigma_A v \rangle > 4 \times 10^{-26}$ cm^3 s^{-1} for a dark matter mass $M_\chi \approx 1$ TeV, when adopting an Einasto profile, within a factor of ∼2 of the thermal cross-section. The HESS GC excludes the light pink PAMELA excess region above $M_\chi \approx 400$ GeV and the Fermi-LAT dwarf analysis excludes the $\tau^+\tau^-$ channel below $M_\chi \approx 400$ GeV, so this model for the PAMELA excess has been ruled out at all dark matter masses when adopting an NFW profile. The red Fermi-LAT feature region is also excluded, at greater than 99.9999% CL, in the $\tau^+\tau^-$ channel for both the Einasto and NFW dark matter profiles, consistent with previous results [7, 10, 12].

For the $4e$ annihilation channel (figure 4(a)), the HESS GC observation constrains the light pink PAMELA excess region of ref. [10] above $M_\chi \approx 600$ GeV for the Einasto halo model, and is constrained above $M_\chi \approx 500$ GeV for the NFW halo model. Similarly, the 4μ annihilation channel (figure 4(b)) has both the light pink region and the light green PAMELA excess region of ref. [22] constrained above $M_\chi \approx 1.5$ TeV for the Einasto halo model, and above $M_\chi \approx 3$ TeV for the NFW halo model.

In the $4e$ channel (figure 4(a)), the purple rectangle shows the range of boost factors for a 1.2 TeV Sommerfeld-enhanced model consistent with the thermal relic density, the CMB, self-interaction bounds, and naturalness, for Δ conservatively from 10^{-4} to unity [37]. Note that the gamma-ray annihilation constraints from the HESS GC on the annihilation cross-section and boost factor, when adopting an NFW or Einasto profile, is often stronger than those from the thermal relic density, the CMB, self-interaction bounds, and naturalness considerations. Specifically, the limits to boosts toward the GC are $B_{GC} \lesssim 27$, which for the comparable central velocity case excludes models with local substructure $\Delta \lesssim 0.025$ (0.17) for $B_{local} = 30$ (50). Our canonical case for $\Delta \approx 0.57$, with GC dark matter velocities comparable to that locally, is unconstrained at 95% CL. Note that any substructure within the inner degree of the HESS GC observation would further enhance these limits due to the corresponding Sommerfeld-enhancement saturation in the GC substructure. The substructure boost in the inner degree has been seen in simulations at the level of $\Delta(r \sim 0.15 \text{ kpc}) \sim 4 \times 10^{-2}$ to 4×10^{-4} [63].

The XDM annihilation models: $\text{Br}(e^+e^-) = \text{Br}(\mu^+\mu^-) = 0.5$, $m_\phi = 0.35$ GeV (figure 5(a)); $\text{Br}(e^+e^-) = \text{Br}(\mu^+\mu^-) = \text{Br}(\pi^+\pi^-) = 0.33$, $m_\phi = 0.58$ GeV (figure 5(b)) ; and, $\text{Br}(e^+e^-) = \text{Br}(\mu^+\mu^-) = 0.25$,$\text{Br}(\pi^+\pi^-) = 0.5$, $m_\phi = 0.90$ GeV (figure 5(c)) are excluded

at greater than 95% CL when adopting an Einasto halo profile. However, when adopting an NFW halo profile, these XDM models have a region from 0.8 TeV $\lesssim M_\chi \lesssim$ 1 TeV below $\langle \sigma_{\rm A} v \rangle \sim 1.8 \times 10^{-24}$ cm^3 s^{-1} which remains consistent at 95% CL.

4 Conclusions

The HESS telescope's observations toward the Galactic center present the strongest constraints on WIMP dark matter annihilation into Standard Model particles for $M_\chi \gtrsim 900$ GeV, given a non-adiabatically-contracted NFW or Einasto profile for the Milky Way dark matter profile. As discussed in the introduction, the HESS GC observation is not sensitive to dark matter annihilation for large constant-density cored dark matter profiles. If such profiles are established to be valid in the Milky Way, the HESS GC observation provides no empirical constraint in these cases given the background subtraction method. If adiabatic contraction and steepening of the dark matter density profile is well established, then the constraints could become stronger. We find that constraints on annihilation into $b\bar{b}$ final states comes within an order of magnitude of the canonical thermal cross section, while $t\bar{t}$ is within a factor of $\sim$20. The $\tau^+\tau^-$ channel is within a factor of $\sim$2 of the thermal cross-section. This bodes well for the future Čerenkov Telescope Array's potential impact at constraining canonical thermal WIMP dark matter this mass scale [73].

We also examine constraints on Sommerfeld-enhanced dark matter annihilation models which produce the PAMELA positron excess and Fermi-LAT e^+e^- spectral feature, including XDM. The models with pure leptonic modes $\tau^+\tau^-$ and $4e$ are excluded at greater than 95% CL by the HESS GC when adopting NFW or Einasto dark matter halo profiles. For other cases, (e.g. 4μ, $2e2\mu$, $e^+e^-\mu^+\mu^-\pi^+\pi^-$), the models are in tension with the HESS GC observations, with portions of the signal 95% CL parameter space are excluded at the 95% CL level. Significantly, the exclusions presented here from HESS GC gamma-ray observations on Sommerfeld-enhanced upper boosts are more constraining, in many cases, than prior constraints from diffuse gamma-rays [38, 39], relic density considerations [28–32], the CMB [29, 33–35], halo shapes [30, 31], and naturalness [36, 37]. In the case where the velocity dispersion of dark matter in the center of the Galaxy is comparable to that locally, the supplemental Sommerfeld-enhancement from local substructure and not at the GC weakens the constraints in certain models.

Gamma-ray astronomy has produced the most stringent constraints on the canonical thermal WIMP model's annihilation cross-section, with Fermi-LAT's stacked observations of dwarf galaxies being the most constraining at low masses, and HESS's observations of the Galactic center being the most constraining at higher masses. With further observation and new technologies, the nature of dark matter may be revealed by gamma-ray telescopes.

Acknowledgments

We thank Prateek Agrawal, Mike Boylan-Kolchin, Oleg Gnedin, Manoj Kaplinghat, Andrey Kravtsov, Mike Kuhlen, Tracy Slatyer and Neal Weiner for useful discussions. KNA & JPH are supported by NSF Grant 07-57966 and NSF CAREER Award 09-55415.

References

[1] F. Zwicky, *Spectral displacement of extra galactic nebulae*, *Helv.Phys.Acta* **6** (1933) 110–127.

[2] J. L. Feng, *Dark Matter Candidates from Particle Physics and Methods of Detection*, *Ann.Rev.Astron.Astrophys.* **48** (2010) 495, [arXiv:1003.0904].

[3] **The HESS** Collaboration, A. Abramowski *et. al.*, *Search for a Dark Matter annihilation signal from the Galactic Center halo with H.E.S.S*, *Phys.Rev.Lett.* **106** (2011) 161301, [arXiv:1103.3266].

[4] **The HESS** Collaboration, J. Hinton, *The Status of the H.E.S.S. project*, *New Astron.Rev.* **48** (2004) 331–337, [astro-ph/0403052].

[5] **The HESS** Collaboration, F. Aharonian *et. al.*, *Discovery of very-high-energy gamma-rays from the galactic centre ridge*, *Nature* **439** (2006) 695–698, [astro-ph/0603021].

[6] M. Regis and P. Ullio, *Multi-wavelength signals of dark matter annihilations at the Galactic center*, *Phys.Rev.* **D78** (2008) 043505, [arXiv:0802.0234].

[7] G. Bertone, M. Cirelli, A. Strumia, and M. Taoso, *Gamma-ray and radio tests of the e+e- excess from DM annihilations*, *JCAP* **0903** (2009) 009, [arXiv:0811.3744].

[8] N. F. Bell and T. D. Jacques, *Gamma-ray Constraints on Dark Matter Annihilation into Charged Particles*, *Phys.Rev.* **D79** (2009) 043507, [arXiv:0811.0821].

[9] G. D. Mack, T. D. Jacques, J. F. Beacom, N. F. Bell, and H. Yuksel, *Conservative Constraints on Dark Matter Annihilation into Gamma Rays*, *Phys.Rev.* **D78** (2008) 063542, [arXiv:0803.0157].

[10] P. Meade, M. Papucci, A. Strumia, and T. Volansky, *Dark Matter Interpretations of the Electron/Positron Excesses after FERMI*, *Nucl. Phys.* **B831** (2010) 178–203, [arXiv:0905.0480].

[11] X.-J. Bi, X.-G. He, E. Ma, and J. Zhang, *Cosmic $e^{\pm}, \bar{p}, \gamma$ and neutrino rays in leptocentric dark matter models*, *Phys.Rev.* **D81** (2010) 063522, [arXiv:0910.0771].

[12] K. N. Abazajian, P. Agrawal, Z. Chacko, and C. Kilic, *Conservative Constraints on Dark Matter from the Fermi-LAT Isotropic Diffuse Gamma-Ray Background Spectrum*, *JCAP* **1011** (2010) 041, [arXiv:1002.3820].

[13] **The HESS** Collaboration, D. Nekrassov, *Searches for DM signals from the Galactic Centre region with H.E.S.S*, arXiv:1106.2752.

[14] A. Geringer-Sameth and S. M. Koushiappas, *Exclusion of canonical WIMPs by the joint analysis of Milky Way dwarfs with Fermi*, arXiv:1108.2914.

[15] **The Fermi-LAT** Collaboration, M. Ackerman *et. al.*, *Constraining dark matter models from a combined analysis of Milky Way satellites with the Fermi-LAT*, arXiv:1108.3546.

[16] O. Adriani *et. al.*, *An anomalous positron abundance in cosmic rays with energies 1.5.100 GeV*, *Nature* **458** (2009) 607–609, [arXiv:0810.4995].

[17] M. Cirelli, M. Kadastik, M. Raidal, and A. Strumia, *Model-independent implications of the e+-, anti-proton cosmic ray spectra on properties of Dark Matter*, *Nucl.Phys.* **B813** (2009) 1–21, [arXiv:0809.2409].

[18] I. Cholis, L. Goodenough, D. Hooper, M. Simet, and N. Weiner, *High Energy Positrons From Annihilating Dark Matter*, *Phys.Rev.* **D80** (2009) 123511, [arXiv:0809.1683].

[19] I. Cholis, D. P. Finkbeiner, L. Goodenough, and N. Weiner, *The PAMELA Positron Excess from Annihilations into a Light Boson*, *JCAP* **0912** (2009) 007, [arXiv:0810.5344].

[20] A. A. Abdo *et. al.*, *Measurement of the Cosmic Ray e+ plus e- spectrum from 20 GeV to 1 TeV with the Fermi Large Area Telescope*, *Phys. Rev. Lett.* **102** (2009) 181101, [arXiv:0905.0025].

[21] I. Cholis, G. Dobler, D. P. Finkbeiner, L. Goodenough, and N. Weiner, *The Case for a 700+ GeV WIMP: Cosmic Ray Spectra from ATIC and PAMELA*, *Phys. Rev.* **D80** (2009) 123518,

[arXiv:0811.3641].

[22] L. Bergstrom, J. Edsjo, and G. Zaharijas, *Dark matter interpretation of recent electron and positron data*, *Phys. Rev. Lett.* **103** (2009) 031103, [arXiv:0905.0333].

[23] **The Fermi-LAT** Collaboration, M. Ackermann *et. al.*, *Measurement of separate cosmic-ray electron and positron spectra with the Fermi Large Area Telescope*, arXiv:1109.0521.

[24] N. Arkani-Hamed, D. P. Finkbeiner, T. R. Slatyer, and N. Weiner, *A Theory of Dark Matter*, *Phys.Rev.* **D79** (2009) 015014, [arXiv:0810.0713].

[25] M. Pospelov and A. Ritz, *Astrophysical Signatures of Secluded Dark Matter*, *Phys.Lett.* **B671** (2009) 391–397, [arXiv:0810.1502].

[26] M. Baumgart, C. Cheung, J. T. Ruderman, L.-T. Wang, and I. Yavin, *Non-Abelian Dark Sectors and Their Collider Signatures*, *JHEP* **0904** (2009) 014, [arXiv:0901.0283].

[27] A. Katz and R. Sundrum, *Breaking the Dark Force*, *JHEP* **0906** (2009) 003, [arXiv:0902.3271].

[28] J. B. Dent, S. Dutta, and R. J. Scherrer, *Thermal Relic Abundances of Particles with Velocity-Dependent Interactions*, *Phys.Lett.* **B687** (2010) 275–279, [arXiv:0909.4128].

[29] J. Zavala, M. Vogelsberger, and S. D. White, *Relic density and CMB constraints on dark matter annihilation with Sommerfeld enhancement*, *Phys.Rev.* **D81** (2010) 083502, [arXiv:0910.5221].

[30] J. L. Feng, M. Kaplinghat, and H.-B. Yu, *Halo Shape and Relic Density Exclusions of Sommerfeld-Enhanced Dark Matter Explanations of Cosmic Ray Excesses*, *Phys.Rev.Lett.* **104** (2010) 151301, [arXiv:0911.0422].

[31] M. R. Buckley and P. J. Fox, *Dark Matter Self-Interactions and Light Force Carriers*, *Phys.Rev.* **D81** (2010) 083522, [arXiv:0911.3898].

[32] J. L. Feng, M. Kaplinghat, and H.-B. Yu, *Sommerfeld Enhancements for Thermal Relic Dark Matter*, *Phys.Rev.* **D82** (2010) 083525, [arXiv:1005.4678].

[33] N. Padmanabhan and D. P. Finkbeiner, *Detecting dark matter annihilation with CMB polarization: Signatures and experimental prospects*, *Phys.Rev.* **D72** (2005) 023508, [astro-ph/0503486].

[34] T. R. Slatyer, N. Padmanabhan, and D. P. Finkbeiner, *CMB Constraints on WIMP Annihilation: Energy Absorption During the Recombination Epoch*, *Phys.Rev.* **D80** (2009) 043526, [arXiv:0906.1197].

[35] J. Hisano, M. Kawasaki, K. Kohri, T. Moroi, K. Nakayama, *et. al.*, *Cosmological constraints on dark matter models with velocity-dependent annihilation cross section*, *Phys.Rev.* **D83** (2011) 123511, [arXiv:1102.4658].

[36] D. P. Finkbeiner, L. Goodenough, T. R. Slatyer, M. Vogelsberger, and N. Weiner, *Consistent Scenarios for Cosmic-Ray Excesses from Sommerfeld-Enhanced Dark Matter Annihilation*, *JCAP* **1105** (2011) 002, [arXiv:1011.3082].

[37] T. R. Slatyer, N. Toro, and N. Weiner, *The Effect of Local Dark Matter Substructure on Constraints in Sommerfeld-Enhanced Models*, arXiv:1107.3546.

[38] K. N. Abazajian, S. Blanchet, and J. P. Harding, *Current and Future Constraints on Dark Matter from Prompt and Inverse-Compton Photon Emission in the Isotropic Diffuse Gamma-ray Background*, arXiv:1011.5090.

[39] J. Zavala, M. Vogelsberger, T. R. Slatyer, A. Loeb, and V. Springel, *The cosmic X-ray and gamma-ray background from dark matter annihilation*, *Phys.Rev.* **D83** (2011) 123513, [arXiv:1103.0776].

[40] J. Hisano, M. Kawasaki, K. Kohri, and K. Nakayama, *Positron/Gamma-Ray Signatures of*

Dark Matter Annihilation and Big-Bang Nucleosynthesis, *Phys.Rev.* **D79** (2009) 063514, [arXiv:0810.1892].

[41] J. Hisano, M. Kawasaki, K. Kohri, T. Moroi, and K. Nakayama, *Cosmic Rays from Dark Matter Annihilation and Big-Bang Nucleosynthesis*, *Phys.Rev.* **D79** (2009) 083522, [arXiv:0901.3582].

[42] D. P. Finkbeiner and N. Weiner, *Exciting Dark Matter and the INTEGRAL/SPI 511 keV signal*, *Phys.Rev.* **D76** (2007) 083519, [astro-ph/0702587].

[43] B. J. Teegarden, K. Watanabe, P. Jean, J. Knodlseder, V. Lonjou, *et. al.*, *INTEGRAL/SPI limits on electron-positron annihilation radiation from the Galactic Plane*, *Astrophys.J.* **621** (2005) 296–300, [astro-ph/0410354].

[44] J. F. Navarro, C. S. Frenk, and S. D. White, *A Universal density profile from hierarchical clustering*, *Astrophys.J.* **490** (1997) 493–508, [astro-ph/9611107].

[45] J. Diemand, M. Kuhlen, P. Madau, M. Zemp, B. Moore, *et. al.*, *Clumps and streams in the local dark matter distribution*, *Nature* **454** (2008) 735–738, [arXiv:0805.1244].

[46] J. Stadel, D. Potter, B. Moore, J. Diemand, P. Madau, M. Zemp, M. Kuhlen, and V. Quilis, *Quantifying the heart of darkness with GHALO - a multibillion particle simulation of a galactic halo*, *Mon. Not. Roy. Astron. Soc.* **398** (Sept., 2009) L21–L25, [arXiv:0808.2981].

[47] J. F. Navarro, A. Ludlow, V. Springel, J. Wang, M. Vogelsberger, S. D. M. White, A. Jenkins, C. S. Frenk, and A. Helmi, *The diversity and similarity of simulated cold dark matter haloes*, *Mon. Not. Roy. Astron. Soc.* **402** (Feb., 2010) 21–34, [arXiv:0810.1522].

[48] G. R. Blumenthal, S. M. Faber, R. Flores, and J. R. Primack, *Contraction of dark matter galactic halos due to baryonic infall*, *Astrophys. J.* **301** (Feb., 1986) 27–34.

[49] O. Y. Gnedin, A. V. Kravtsov, A. A. Klypin, and D. Nagai, *Response of dark matter halos to condensation of baryons: Cosmological simulations and improved adiabatic contraction model*, *Astrophys.J.* **616** (2004) 16–26, [astro-ph/0406247].

[50] S. Pedrosa, P. B. Tissera, and C. Scannapieco, *The joint evolution of baryons and dark matter haloes*, *Mon. Not. Roy. Astron. Soc.* **402** (Feb., 2010) 776–788, [arXiv:0910.4380].

[51] P. B. Tissera, S. D. M. White, S. Pedrosa, and C. Scannapieco, *Dark matter response to galaxy formation*, *Mon. Not. Roy. Astron. Soc.* **406** (Aug., 2010) 922–935, [arXiv:0911.2316].

[52] J. Guedes, S. Callegari, P. Madau, and L. Mayer, *Forming Realistic Late-Type Spirals in a LCDM Universe: The Eris Simulation*, *Astrophys.J.* **742** (2011) 76, [arXiv:1103.6030].

[53] O. Y. Gnedin, D. Ceverino, N. Y. Gnedin, A. A. Klypin, A. V. Kravtsov, *et. al.*, *Halo Contraction Effect in Hydrodynamic Simulations of Galaxy Formation*, arXiv:1108.5736.

[54] E. Romano-Díaz, I. Shlosman, Y. Hoffman, and C. Heller, *Erasing Dark Matter Cusps in Cosmological Galactic Halos with Baryons*, *Astrophys. J. Lett.* **685** (Oct., 2008) L105–L108, [arXiv:0808.0195].

[55] E. Romano-Diaz, I. Shlosman, C. Heller, and Y. Hoffman, *Dissecting Galaxy Formation: I. Comparison Between Pure Dark Matter and Baryonic Models*, *Astrophys.J.* **702** (2009) 1250–1267, [arXiv:0901.1317].

[56] A. V. Maccio', G. Stinson, C. B. Brook, J. Wadsley, H. Couchman, *et. al.*, *Halo expansion in cosmological hydro simulations: towards a baryonic solution of the cusp/core problem in massive spirals*, arXiv:1111.5620.

[57] H. Zhan, *Optimal Softening for N-Body Halo Simulations*, *Astrophys.J.* **639** (2006) 617–620, [astro-ph/0507237].

[58] C. Power, J. Navarro, A. Jenkins, C. Frenk, S. D. White, *et. al.*, *The Inner structure of Lambda CDM halos. 1. A Numerical convergence study*, *Mon.Not.Roy.Astron.Soc.* **338** (2003) 14–34,

[astro-ph/0201544].

[59] G. S. Stinson, J. Bailin, H. Couchman, J. Wadsley, S. Shen, S. Nickerson, C. Brook, and T. Quinn, *Cosmological galaxy formation simulations using smoothed particle hydrodynamics*, *Mon. Not. Roy. Astron. Soc.* **408** (Oct., 2010) 812–826, [arXiv:1004.0675].

[60] **The HESS** Collaboration, F. Aharonian *et. al.*, *The H.E.S.S. survey of the Inner Galaxy in very high-energy gamma-rays*, *Astrophys. J.* **636** (2006) 777–797, [astro-ph/0510397].

[61] L. Pieri, J. Lavalle, G. Bertone, and E. Branchini, *Implications of High-Resolution Simulations on Indirect Dark Matter Searches*, *Phys. Rev.* **D83** (2011) 023518, [arXiv:0908.0195].

[62] R. Catena and P. Ullio, *A novel determination of the local dark matter density*, *JCAP* **1008** (2010) 004, [arXiv:0907.0018].

[63] M. Kuhlen, J. Diemand, and P. Madau, *The Dark Matter Annihilation Signal from Galactic Substructure: Predictions for GLAST*, *Astrophys. J.* **686** (Oct., 2008) 262–278, [arXiv:0805.4416].

[64] T. Sjostrand, S. Mrenna, and P. Z. Skands, *PYTHIA 6.4 Physics and Manual*, *JHEP* **0605** (2006) 026, [hep-ph/0603175].

[65] **Particle Data Group** Collaboration, K. Nakamura *et. al.*, *Review of particle physics*, *J.Phys.G* **G37** (2010) 075021.

[66] J. Mardon, Y. Nomura, D. Stolarski, and J. Thaler, *Dark Matter Signals from Cascade Annihilations*, *JCAP* **0905** (2009) 016, [arXiv:0901.2926].

[67] P. Grajek, G. Kane, D. J. Phalen, A. Pierce, and S. Watson, *Neutralino Dark Matter from Indirect Detection Revisited*, arXiv:0807.1508.

[68] M. Cirelli, P. Panci, and P. D. Serpico, *Diffuse gamma ray constraints on annihilating or decaying Dark Matter after Fermi*, *Nucl.Phys.* **B840** (2010) 284–303, [arXiv:0912.0663].

[69] M. Kamionkowski, S. M. Koushiappas, and M. Kuhlen, *Galactic Substructure and Dark Matter Annihilation in the Milky Way Halo*, *Phys.Rev.* **D81** (2010) 043532, [arXiv:1001.3144].

[70] J. F. Navarro *et. al.*, *The Inner Structure of LambdaCDM Halos III: Universality and Asymptotic Slopes*, *Mon. Not. Roy. Astron. Soc.* **349** (2004) 1039, [astro-ph/0311231].

[71] M. Boylan-Kolchin, C.-P. Ma, and E. Quataert, *Dissipationless mergers of elliptical galaxies and the evolution of the fundamental plane*, *Mon.Not.Roy.Astron.Soc.* **362** (2005) 184–196, [astro-ph/0502495].

[72] I. Cholis and N. Weiner, *MiXDM: Cosmic Ray Signals from Multiple States of Dark Matter*, arXiv:0911.4954.

[73] The CTA Consortium, *Design Concepts for the Cherenkov Telescope Array*, arXiv:1008.3703.

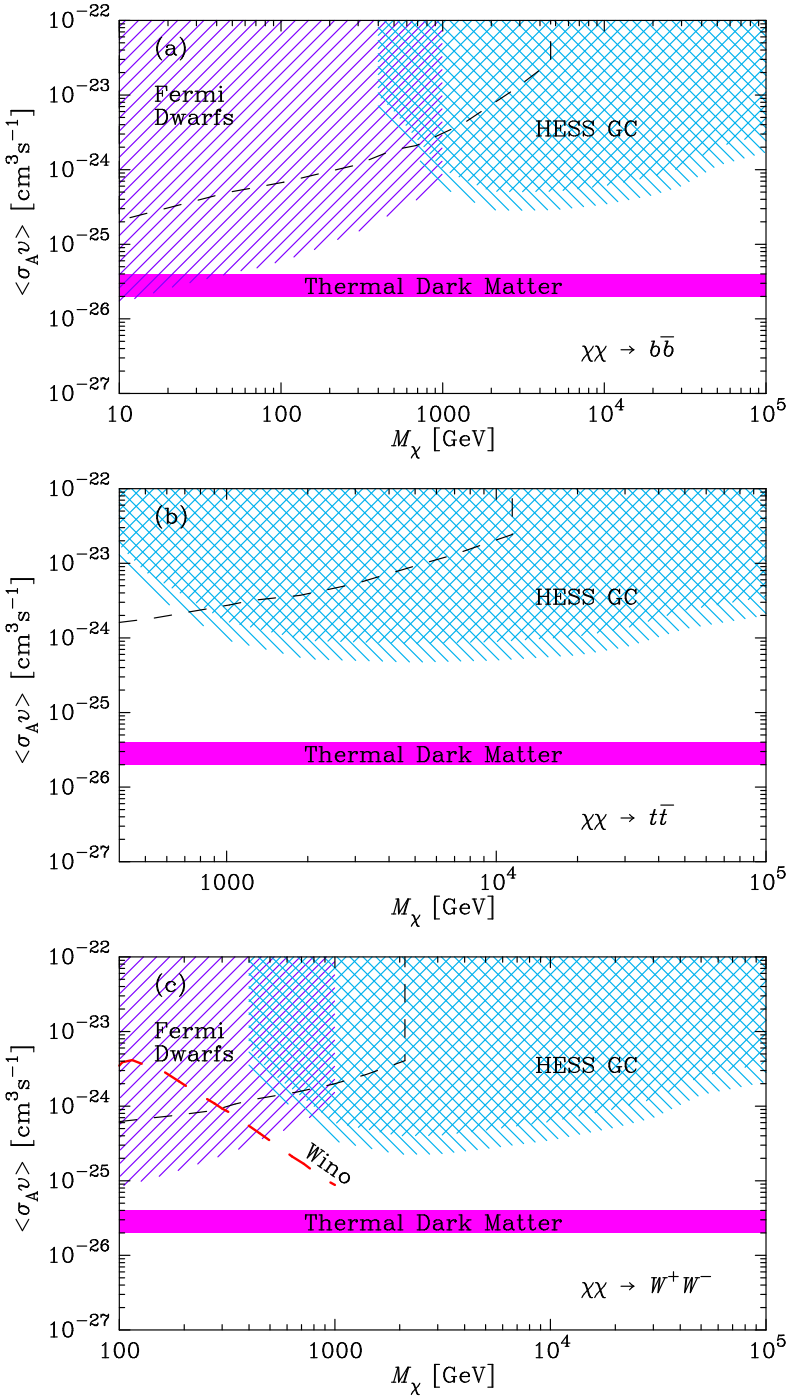

Figure 2. Shown are the constraints on dark matter in three canonical annihilation channels: (a) $b\bar{b}$; (b) $t\bar{t}$; (c) W^+W^-. The regions are labeled according to their constraining observations as described in the text: "HESS GC" are the 95% CL limits from the HESS analysis of the GC. The double hatched region is constrained for both the Einasto and NFW halo models, and the single hatched region is constrained for only the Einasto halo model. The regions labeled "Fermi Dwarfs" are the 95% CL limits from the Fermi-LAT collaboration analysis of dwarf spheroidals. In the W^+W^- channel, panel (c), the mass for a non-thermal wino-like neutralino is shown as a thick-dashed red line [67]. For comparison, we plot the 3σ limits from ref. [68] for their analysis of the Fermi-LAT observation of the $3^\circ \times 3^\circ$ region around the Galactic Center as dashed (black) lines in all panels for the respective channels.

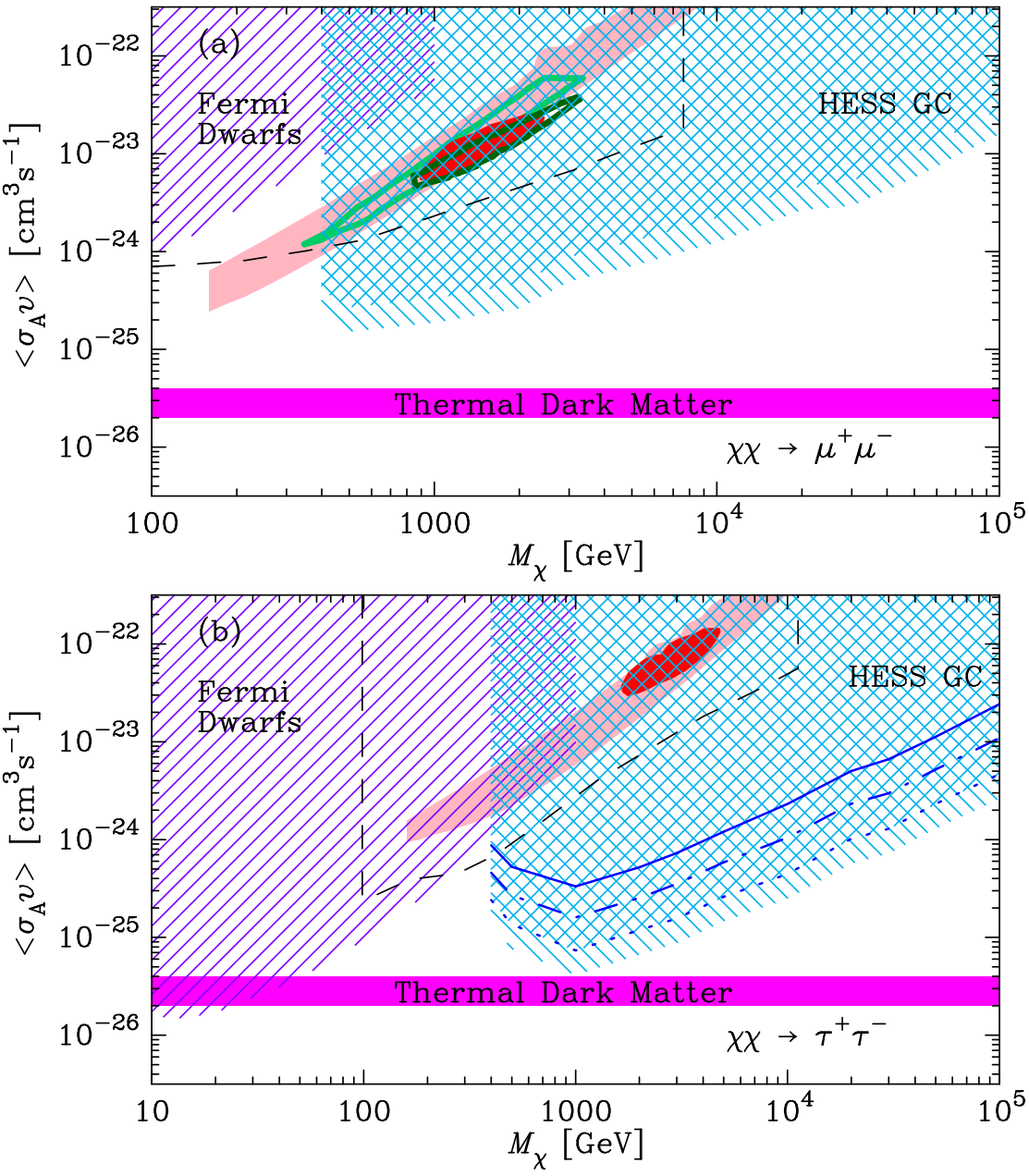

Figure 3. Shown are the constraints on dark matter in two leptonic annihilation channels: (a) $\mu^+\mu^-$; (b) $\tau^+\tau^-$. The regions are labeled according to their constraining observations as described in the text: "HESS GC" are the 95% CL limits from the HESS analysis of the GC. The double hatched region is constrained for both the Einasto and NFW halo models, and the single hatched region is constrained for only the Einasto halo model. The regions labeled "Fermi Dwarfs" are the 95% CL limits from the Fermi-LAT collaboration analysis of dwarf spheroidals. The light pink shaded region is consistent with a dark matter interpretation of the PAMELA signal and the dark red shaded region is that from the Fermi-LAT e^+e^- feature from ref. [10]. In the $\mu^+\mu^-$ channel, panel (a), the light green outlined region is consistent with a dark matter interpretation of the PAMELA signal and the dark green outlined region with that of the Fermi-LAT e^+e^- feature from ref. [22]. PAMELA regions below $M_\chi = 160$ GeV are ruled out by the rise in the positron fraction seen by the Fermi-LAT [23]. In panel (b), to illustrate the strength of the HESS GC limits, we show for the NFW profile the 95%, 99.7% and 99.9999% CL limits in dotted, dot-dashed and solid lines, respectively. For comparison, we plot the 3σ limits from ref. [68] for their analysis of prompt and inverse-Compton emission in the Fermi-LAT observation of the $3^\circ \times 3^\circ$ region around the Galactic Center as dashed (black) lines in both panels for the respective channels.

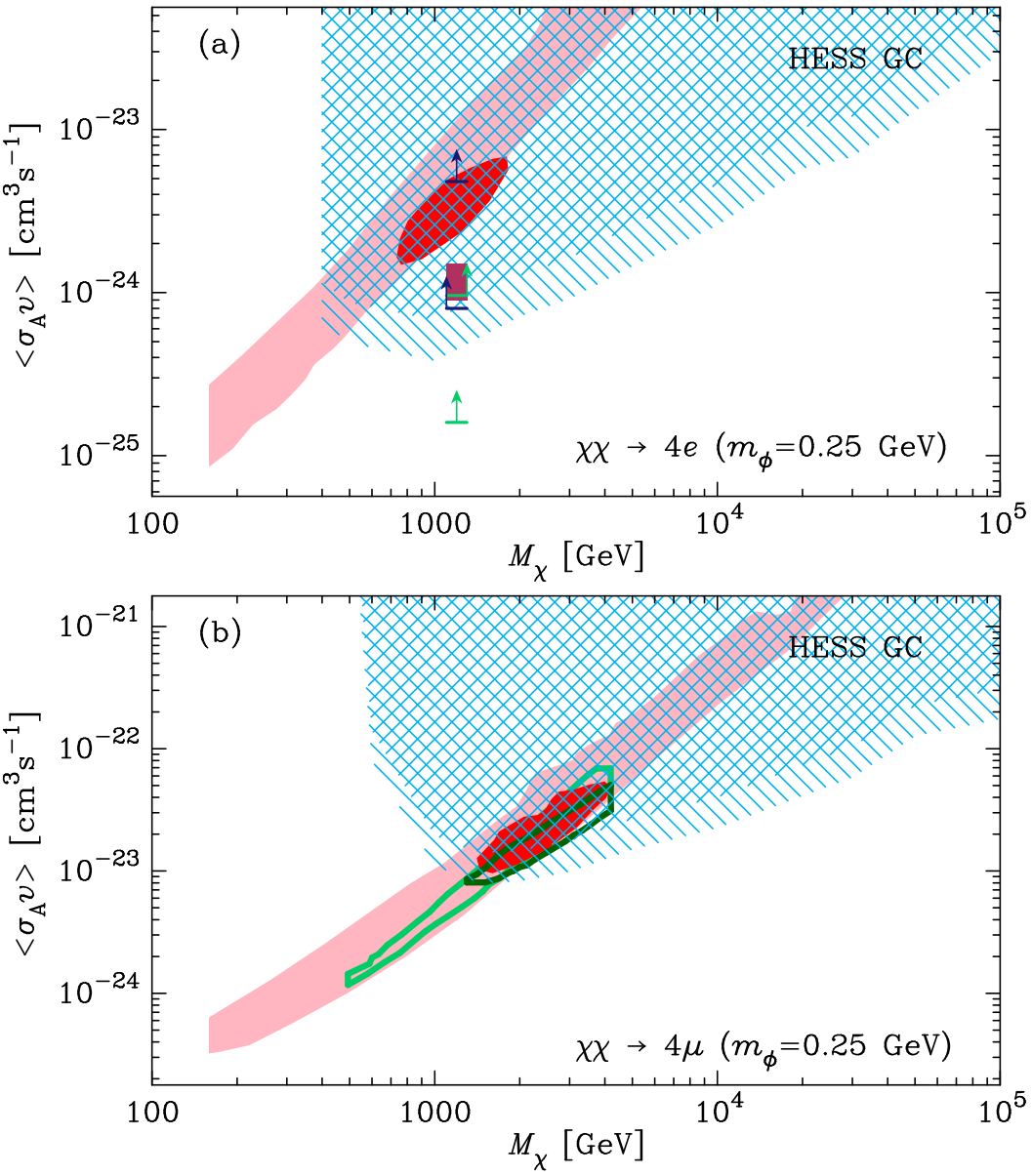

Figure 4. Shown are the constraints on dark matter in two annihilation channels: (a) annihilation into two e^+e^- pairs via two intermediate 0.25 GeV gauge bosons ϕ (note that this case requires an *ad hoc* requirement of decay into electrons and not muons); (b) annihilation into two μ^+ and two μ^- via two intermediate 0.25 GeV gauge bosons ϕ. The regions are labeled according to their constraining observations as described in the text: "HESS GC" are the 95% CL limits from the HESS analysis of the GC. The double hatched region is constrained for both the Einasto and NFW halo models, and the single hatched region is constrained for only the Einasto halo model. The light pink shaded region is consistent with a dark matter interpretation of the PAMELA signal and the dark red shaded region is that of the Fermi-LAT e^+e^- feature from ref. [10]. In the $4e$ channel, panel (a), the purple rectangle demonstrates the range of Sommerfeld-enhanced cross-sections consistent with constraints from thermal relic density, the CMB, self-interaction bounds, and naturalness [37]. The green (blue) bars and arrows show the HESS GC limits for the two cases of velocity dispersions of $v \rightarrow 0$ ($v \sim 150$ km s^{-1}), respectively, with the upper and lower bars for each color representing the two local substructure boost limits, as described in the text. In the 4μ channel, panel (b), the light green outlined region is consistent with a dark matter interpretation of the PAMELA signal and the dark green outlined region is that for Fermi-LAT e^+e^- feature from ref. [22]. PAMELA regions below $M_\chi \approx 160$ GeV are ruled out by the rise in the positron fraction seen by the Fermi-LAT [23].

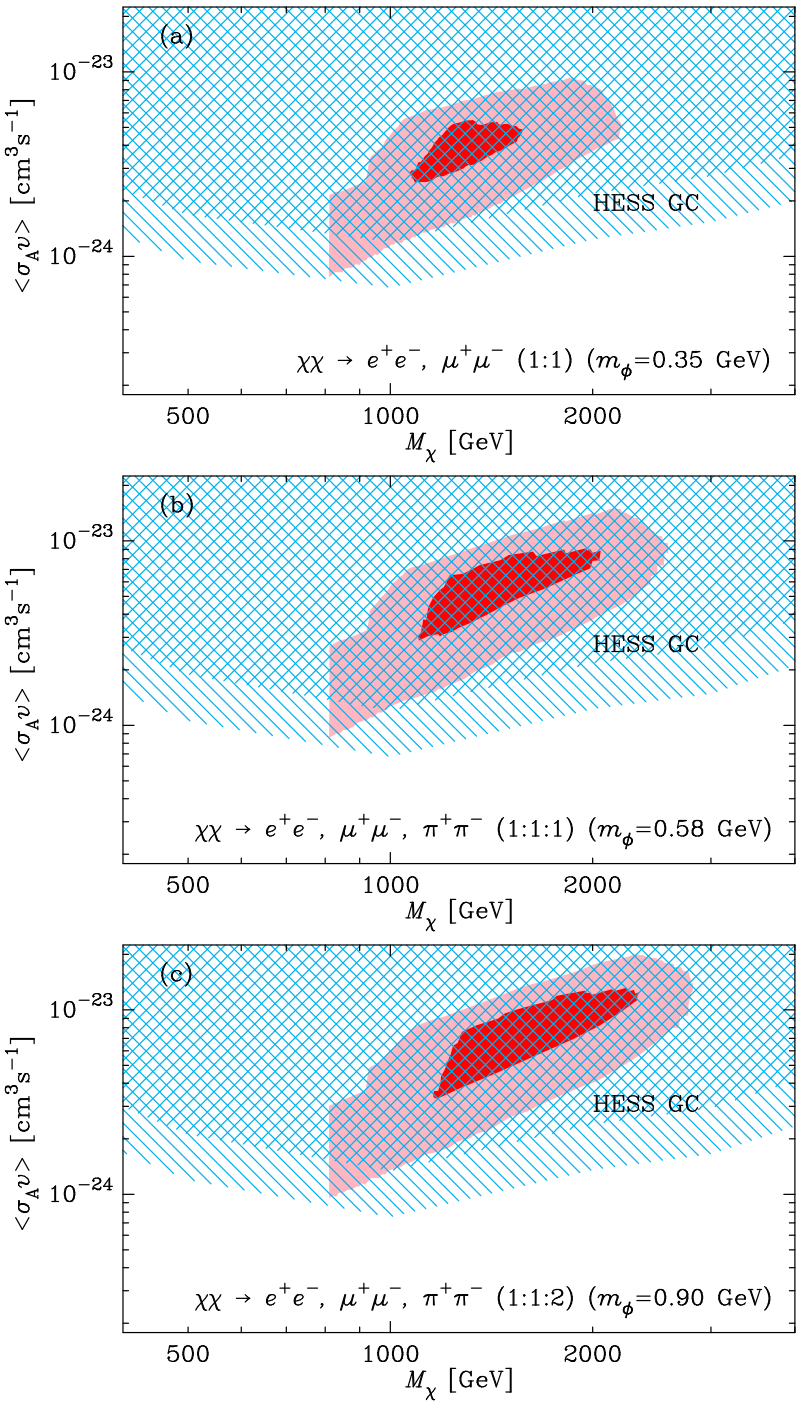

Figure 5. Shown are the constraints on dark matter in three XDM annihilation cases: (a) annihilation into 50% e^+e^- and 50% $\mu^+\mu^-$ via two intermediate 0.35 GeV gauge bosons ϕ; (b) annihilation into 33% e^+e^-, 33% $\mu^+\mu^-$, and 33% $\pi^+\pi^-$ via two intermediate 0.58 GeV gauge bosons ϕ; (c) annihilation into 25% e^+e^-, 25% $\mu^+\mu^-$, and 50% $\pi^+\pi^-$ via two intermediate 0.90 GeV gauge bosons ϕ. The regions are labeled according to their constraining observations as described in the text: "HESS GC" are the 95% CL limits from the HESS analysis of the GC. The double hatched region is constrained for both the Einasto and NFW halo models, and the single hatched region is constrained for only the Einasto halo model. The light pink and dark red shaded regions are the 68% and 95% CL regions consistent with the XDM dark matter interpretation of a combination of the PAMELA signal and the Fermi-LAT e^+e^- feature from ref. [36].